Arabian Journal of Chemistry (2022) **15**, 103894

King Saud University

Arabian Journal of Chemistry

www.ksu.edu.sa
www.sciencedirect.com

ORIGINAL ARTICLE

Exploration of spray pyrolysis technique in preparation of absorber material CFATS: Unprecedented hydrophilic surface and antibacterial properties

Chayma Nefzi [a,*], **Bechir Yahmadi** [a,b,*], **M. Lahmar** [c], **H.I. Ouzari** [c], **Nizar El Guesmi** [d], **Jorge M. García** [e], **Najoua Kamoun-Turki** [a], **Saleh A. Ahmed** [d,f,*]

[a] *Université Tunis El Manar, Faculté des Sciences de Tunis, Département de Physique, LR99ES13 Laboratoire de Physique de la Matière Condensée (LPMC), 2092 Tunis Tunisie, Tunisia*
[b] *Physics Department, Common First Year Deanship, Umm Al-Qura University, Makkah 21955, Saudi Arabia*
[c] *Laboratoire de Microorganismes et Biomolecules Actives, Faculté des sciences de Tunis, Université Tunis El Manar, 2092 Tunis, Tunisia*
[d] *Department of Chemistry, Faculty of Applied Science, Umm Al-Qura University, 21955 Makkah, Saudi Arabia*
[e] *Instituto de Micro y Nanotecnología CNM, CSIC. Calle Isaac Newton, 8. Tres Cantos, 28760 Madrid, Spain*
[f] *Chemistry Department, Faculty of Science, Assiut University, 71516 Assiut, Egypt*

Received 3 January 2022; accepted 3 April 2022
Available online 13 April 2022

KEYWORDS

$Cu_2Fe1-xAlxSnS_4$ films;
Spray pyrolysis;
Antibacterial activity;
Hydrophilicity

Abstract In this study, we achieve the production of nontoxic $Cu_2Fe_{1-x}Al_xSnS_4$ films ($x = 0, 0.25, 0.50, 0.75$ and 1) by substituting Fe with Al atoms. Physical properties of the investigated films were studied using: Energy dispersive X-ray spectrometry (EDX), scanning electron microscopy (SEM), X-ray diffraction (XRD), Raman spectroscopy, spectrophotometer and drop shape analysis system (DSA). The formation of new quaternary $Cu_3Al_{0.6}Sn_1S_6$ (CATS) chalcogenide for $x = 1$ was proven from EDX study. Notably, the major diffraction peaks were located at $2\theta = 28.34°, 47.43°$ and $55.93°$ which are respectively tagged as (1 1 2), (2 0 4), and (3 1 2) plans, confirming the stannite crystal structure of $Cu_3Al_{0.6}Sn_1S_6$ film. The morphological states show a nanofiber structure accompanied with voids and cavities for CATS films. Tauc-relation plot reveals direct energy bandgap, close

---

[*] Corresponding authors at: Université Tunis El Manar, Faculté des Sciences de Tunis, Département de Physique, LR99ES13 Laboratoire de Physique de la Matière Condensée (LPMC), 2092 Tunis Tunisie, Tunisia (C. Nefzi); Physics Department, Common First Year Deanship, Umm Al-Qura University, Makkah 21955, Saudi Arabia (B. Yahmadi); Department of Chemistry, Faculty of Applied Science, Umm Al-Qura University, 21955 Makkah, Saudi Arabia (S.A. Ahmed).
E-mail addresses: nefzichaima@fst.utm.tn (C. Nefzi), bmyahmadi@uqu.edu.sa (B. Yahmadi), saahmed@uqu.edu.sa (S.A. Ahmed).

Peer review under responsibility of King Saud University.

ELSEVIER **Production and hosting by Elsevier**

https://doi.org/10.1016/j.arabjc.2022.103894

to 1.52 eV, which proves the absorber film type of $Cu_3Al_{0.6}Sn_1S_6$. The effluent toxicity of the obtained thin films has been assessed using the inhibition of Gram-positive (*Staphylococcus aureus*) and Gram-negative (*Escherichia coli*) bacteria and indicated good antibacterial activity of the CATS/SnO_2:F heterojunction. The viability rates against *S. aureus* achieved 40 %, 31 % and 15% for SnO_2:F, $Cu_3Al_{0.6}Sn_1S_6$ films and CATS/SnO_2:F heterojunction. These results highlight the great antibacterial activity of coupled CATS/SnO_2:F. Therefore this research underscores the effectiveness of CATS/SnO_2:F surface which demonstrates self-disinfecting and self-cleaning with hydrophilicity and high antibacterial activity.

1. Introduction

The I-III-VI semiconductors with chalcogenide structure have sparked great interest owning to their good semiconducting and optical properties useful for optoelectronic and biomedicine applications (Koç et al., 2021; Shin et al., 2013; Mokurala et al., 2016; Ozel, 2016; Ali et al., 2020). Much research has been dedicated to the exploration of abundant and low-cost semiconductors to produce renewable and clean energy for solar cells (Betul et al., 2021; Benyahia et al., 2021; Sadanand et al., 2021; Khemiri et al., 2020; Hussein et al., 2021; Victoria et al., 2021; Sun et al., 2021). In recent years, CdTe and Cu (In,Ga)Se_2 (CIGSe) have been used as effective absorbers which may be engineered and tuned for solar cells with high power conversion efficiency (Shin et al., 2022; Amoupour et al., 2021). Nevertheless, the expensive cost and scarcity of In, Ga and Te elements and the toxicity of Cd present major issues that limit the widespread fabrication of CdTe and CIGS semiconductors. Quaternary I_2–II–IV–VI_4 (I = Cu, Ag, II = Fe, Zn, Mn, Cd, IV = Si, Ge, Sn, VI = S, Se, Te) chalcogenides create a large group of semiconductors with different structural, optical, and electrical properties. Among them, Cu_2MgSnS_4, Cu_2FeSnS_4, Cu_2InSnS_4 and Cu_2CoSnS_4 semiconductors have recently emerged as promising light-absorber semiconductors for solar cells to replace the remarkable properties of CIGS (Shin et al., 2022; Amoupour et al., 2021; Nefzi et al., 2021a; Nefzi et al., 2021b; Nefzi et al., 2020a; Nefzi et al., 2020b).

In addition, wetting behavior is one of the most influential surface properties of a solid and therefore is of great relevance in many applications from both practical and fundamental point of view. The water contact angle θ (WCA) determines the surface wettability by the angle between solid/air and liquid/air interfaces. Taking advantages of their properties, hydrophilicity and hydrophobicity impact applications including self-cleaning (Wan et al., 2011), antimicrobial property (Kim et al., 2021; Sopata et al., 2020), medical supplies (Sui et al., 2020), and friction reduction (Wang et al., 2011).

A relevant field of applications involves using nanoparticles semiconductors as bactericides and insecticides (Shin et al., 2022; De Falco et al., 2018; Qi et al., 2019; Karam et al., 2013). Nanomaterials exhibiting antimicrobial property can be used for the purpose of combatting the proliferation of pathogenic microorganisms such as bacteria and fungi. Based on literature, Gram-negative bacteria present less resistance against nanoparticles material than Gram-positive ones (Naderi et al., 2020). The Gram-negative bacteria *Escherichia coli (E.coli)* is a cause of concern for humanity and the Gram-positive bacteria *Staphylococcus aureus* (*S. aureus*) is responsible for food poisoning, hospital infections, ulcers, skin infections and abdominal abscesses (Davarpanah et al., 2022).

In this work, we report, for the first time, on new promising candidate $Cu_2Fe_{1-x}Al_xSnS_4$ (CFATS) thin films using spray pyrolysis technique (for x = 0, 0.25, 0.50, 0.75 and 1) where × is the ratio of between Al and Fe concentration in the spray solution (x = $[Al^{3+}]$/ $[Fe^{3+}]$). We have synthesized absorber CATS film with direct band gap and studied the surface wettability of CFATS. Then, the antimicrobial activities of SnO_2:F, CATS and CATS/SnO_2:F against *Staphylococcus aureus* and *Escherichia coli* were investigated. The overarching aim of our research is to explore the physical properties of novel material for different applications like biomaterials.

2. Experimental

2.1. Chemicals

Copper (II) chloride dihydrate ($CuCl_2{\cdot}2H_2O$, 99.99%), aluminum (III) chloride hexahydrate ($AlCl_3{\cdot}6H_2O$, 95%), iron (III) chloride hexahydrate ($FeCl_3$, $6H_2O$, 0.004 M), tin (II) chloride dehydrate ($SnCl_2$, $2H_2O$, 98%) and thiourea (CH_2N_2-S, 98%) were purchased from Sigma Aldrich and Fluka. All chemicals products were used without any further purification for the elaboration of Cu_2Fe_{1-x} Al_xSnS_4 (CFATS) thin layers. The methanol (CH_4O, 99.99%) was purchased from Fisher Chemical society and used as a solvent.

2.2. Deposition of Cu_2Fe_{1-x} Al_xSnS_4 (CFATS) thin films

$Cu_2Fe_{1-x}Al_xSnS_4$ (CFATS) thin films deposited on glass substrates using chemical spray pyrolysis technique in ambient air. The glass substrates were cleaned in ultrasonic bath using double-distilled water (Bi-distiller water GFL), followed by isopropyl alcohol for 10 min. All cleaned substrates were dried in a furnace at 80 °C for 15 min. Typically, the sprayed solution was prepared by mixing $CuCl_2$ (0.01 M), $AlCl_3$ (0.004 M), $FeCl_3$ (0.004 M), $SnCl_2$ (0.004 M) and CH_2N_2S (0.04 M) in 300 ml of methanol. This process was repeated three times to obtain approximately good physical properties. Then, the solutions were varied with and without aluminum concentrations by maintaining × = 0, 0.25, 0.50, 0.75, and 1 for the growth of Cu_2Fe_{1-x} Al_xSnS_4 layers. The obtained solutions were stirred for 15 min until they became clear and transparent without impurities which can potentially block the nozzle of the sprayer. Therefore, this solution is sprayed with a flow rate of 25 ml/min onto preheated substrates

(T_s = 240 °C) as fine droplets by means of compressed air as carrier gas. The substrates and nozzle distance is equal to 28 cm. The possible proposed growth mechanism may follow the reactions as follows (Orletskii et al., 2018):

$$2Cu^{2+} + Sn^{2+} \rightarrow 2Cu^{+} + Sn^{4+}$$

$$Cu^{+} + Cl^{-} \rightarrow CuCl$$

$$CuCl + 2SC(NH_2)_2 \rightarrow [Cu(SC(NH_2)_2)_2]Cl$$

$$Sn^{4+} + 2SC(NH_2)_2 \rightarrow [Sn(SC(NH_2)_2)_2]^{4+}$$

$$Al^{3+} + 2SC(NH_2)_2 \rightarrow [Al(SC(NH_2)_2)_2]^{3+}$$

The formation of CATS is the result of the following reaction:

$$Cu(SC(NH_2)_2)_2]^{+} + [Sn(SC(NH_2)_2)_2]^{4+} + [Al(SC(NH_2)_2)_2]^{2+} \rightarrow Cu_2AlSnS_4 \text{ precursor solution.}$$

2.3. Bacterial adhesion analysis

Basically, the Gram-negative bacterium *Escherichia coli* (*E.-coli*) and the Gram-positive bacterium *Staphylococcus aureus* (*S. aureus*) have been utilized as the experimental strains by counting forming unity (CFU). Overnight the growth of *E. coli* and *S. aureus* were attained at 37 °C in 5 ml of Tryptic Soya Broth (TSB) medium under agitation. Spread 10 µl of each culture on the chemically coated thin films and other uncoated glass slides that will serve as a control (previously sterilized in glass petri dishes) make a series of dilutions of the two cultures to spread it and count it on Tryptic Soya Agar TSA (up to 10^{-6} is sufficient). Incubate the slides at 37 °C for 48 h, taking care not to tip them over when moving to the oven. After 48 h, immerse each film in Eppendorf tube filled with 1 ml of physiological water (using sterile forceps without touching the surface on which you have deposited the culture) and vortex it well to detach the slide bacteria. Therefore, this is a stock solution. Carry out successive dilutions and spread on (TSA) for enumeration. Also, spread 100 µl of the stock solution (normally a dilution up to 10^{-4} is sufficient). The decrease in CFU/mL is considered as the effect of thin films against the bacterial growth. Calculate the viability (%) with the following formula;

$$\mathbf{Viability}(\%) = \frac{\mathbf{CFU\ offilms}}{\mathbf{CFU\ of\ the\ control}} * 100 \tag{1}$$

2.4. Characterization methods

The crystalline phases were studied using an XPERT-PRO diffractometer system with λ = 1.5406 Å and 2θ varied from 20° to 60° at room temperature. The purity of films was investigated by Raman spectrometer type Jobin Yvon technology T 64,000 with 488 nm argon in laser like excitation source. Elemental compositions were explored using Energy dispersive X-ray spectroscopy (EDX). Film morphology and thickness was examined using scanning electron microscopy (SEM) type Zeiss EVO MA10 microscope. Optical behavior was recorded using spectrophotometer type Perkin Elmer Lambda 950 in the wavelength range 250–2500 nm at room temperature. The surface wettability of $Cu_2Fe_{1-x}Al_xSnS_4$ (x = 0, 0.25, 0.50, 0.75 and 1) thin films were investigated by Water Contact angle θ (WCA) measurements using Drop Shape Analysis System type DSA100 (Kruss GmbH, Hamburg).

3. Results and discussion

3.1. Chemical composition

The composition of synthesized $Cu_2Fe_{1-x}Al_xSnS_4$ thin layers (x = 0–0.25 – 0.50–0.75 and 1) has been determined using energy-dispersive X-ray (EDX) spectroscopy and the results are provided in Table 1. This table indicates the existence of copper, iron, aluminum, tin and sulfur comprising the $Cu_2Fe_{1-x}Al_xSnS_4$ molecular structure. As expected, the rise in aluminum concentration seems to change the elemental composition of Cu, Sn and S contents in the films. It is shown that copper and tin amounts increased with Al inclusion. Fig. 1 shows the elements composition of $Cu_2Al_xSnS_4$ (where x = 1) thin layer. Moreover, copper, aluminum, tin and sulfur ratios in Cu_2AlSnS_4 (where x = 1) are about 28.7: 5.92: 10.38: 54.99, which are nearly in accordance with the stoichiometric ratio of $Cu_3Al_{0.6}Sn_1S_6$ (CATS) composition.

3.2. Structural characterization

The crystallographic structure of $Cu_2Fe_{1-x}Al_xSnS_4$ thin layers (x = 0–0.25 – 0.50–0.75 and 1) has been studied by XRD with Cu (kα) radiation source in the range of 2θ [10°-70°] as shown in Fig. 2. The major diffraction peaks 2θ = 18.20°, 28.77°, 47.86° and 56.87° were indexed respectively to (0 0 2), (1 1 2), (2 0 4), and (3 1 2) plans of stannite CFTS structure, coordinated with the standard (JCPDF card No. 74-1025). In stannite structure the space group is I $\bar{4}$ 2 m, each atom has four nearest neighbors and each anion S is surrounded by two Cu one Fe and one Sn atoms. On the other hand, each cation is tetrahedrally coordinated by four anions. After aluminum inclusion in $Cu_2Fe_{1-x}Al_xSnS_4$ (CFATS) matrix, the peak intensities are slightly decreased accompanied with broad full width at half-maximum (FWHM), designed a decline of the crystallinity. The poor crystalline quality at x = 0.25 indicates that some quantities of Al atoms prefer to situate in or near the grain boundary regions (Venkatachalam et al., 2008). Meanwhile, the large FWHM may be originated to a combination of grains and possible assembling of the micro-strains at several planes as crytallographic defects form (Das Bakshi et al., 2018). It is also evidenced that all peaks are shifted

Table 1 Average chemical composition values at four aluminum concentrations (x = 0 – 0.25 – 0.50–0.75 and 1).

x	$\frac{Cu}{Fe+Al+Sn}$	$\frac{Fe}{Sn}$	$\frac{Al}{Sn}$	$\frac{S}{metal}$
0	0.96	0.82	—	0.90
0.25	1.32	0.17	0.60	0.80
0.50	1.74	0.41	0.25	0.84
0.75	1.58	0.50	0.41	0.78
1	1.76	—	0.57	1.20

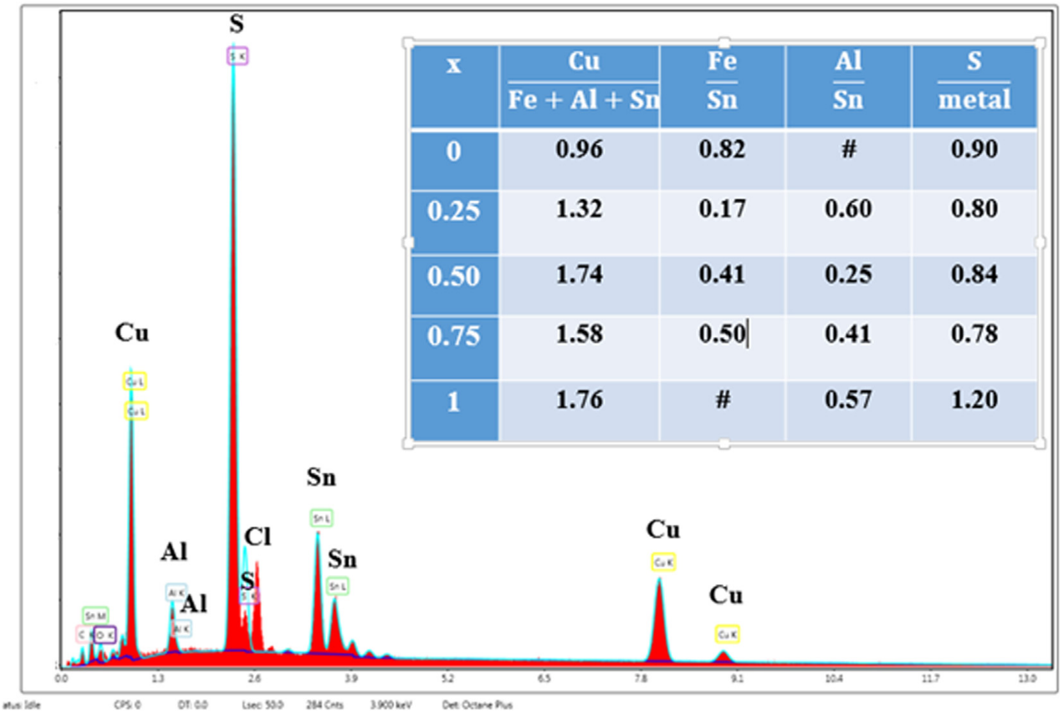

x	$\frac{Cu}{Fe+Al+Sn}$	$\frac{Fe}{Sn}$	$\frac{Al}{Sn}$	$\frac{S}{metal}$
0	0.96	0.82	#	0.90
0.25	1.32	0.17	0.60	0.80
0.50	1.74	0.41	0.25	0.84
0.75	1.58	0.50	0.41	0.78
1	1.76	#	0.57	1.20

Fig. 1 EDAX spectrum of CATS (where x = 1) film.

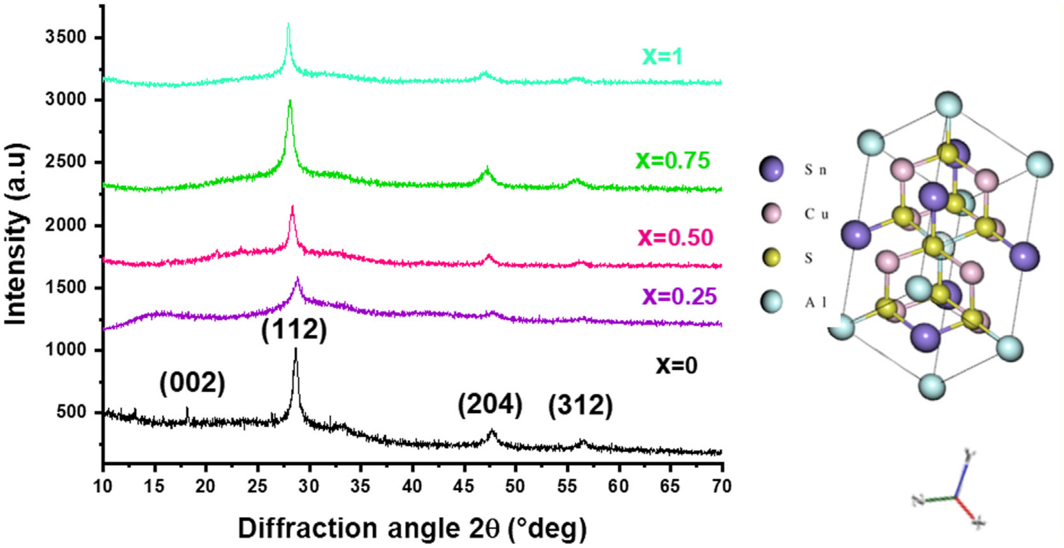

Fig. 2 XRD patterns of $Cu_2Fe_{1\text{-}x}Al_xSnS_4$ films (x = 0–0.25 – 0.50–0.75 and 1) films. Inset presents the Stannite Type Structure of CATS material.

toward lower angles, which is due to an increment of lattice parameters for CFATS materials. This trend may be ascribed to the ionic radii of Al^{3+} (0.53 Å) that is lower to that of Fe^{3+} (0.64 Å). However, for x = 1, the patterns of CATS thin film revealed a polycrystalline nature with diffraction peaks 2θ = 28.34°, 47.43° and 55.93° that are identified respectively to (112), (204), and (312) plans. No sign of contamination CATS thin film.

Crystallite size (D), dislocation density (δ_{dis}), crystallites number (Nc) and strain (ε) were calculated for (112) plane using the following relations (Monisha et al., 2021; Agawane et al., 2014) and tabulated in Table 2:

$$\mathbf{D} = \frac{\mathbf{K}.\lambda}{\beta.\mathbf{cos}\theta}\delta_{\mathbf{dis}} = \frac{1}{\mathbf{D}^2}, \mathbf{N_c} = \frac{\mathbf{e}}{\mathbf{D}^3}, \boldsymbol{\varepsilon} = \frac{\boldsymbol{\beta}\mathbf{cos}(\boldsymbol{\theta})}{4} \tag{2}$$

Where: k is the shape factor, λ is the wavelength of incident X-ray, β is the full-width at half maximum, e is the film thickness and θ is the Bragg angle. The average crystallite size decreases from 60 nm for CFTS film to 45 nm for CATS film. This trend suggests the high crystallinity at x = 1 than the

Table 2 Experimental crystal parameters of $Cu_2Fe_{1\text{-}x}Al_xSnS_4$ ($0 \leq x \leq 1$) films: Crystallite size (D), dislocation density (δ_{dis}), number of crystallites (Nc), lattice parameters (a and c) and the strain (ε).

x	0	0.25	0.50	0.75	1
D (nm)	60	23	19	19	45
δ_{dis} (10^{11} cm^{-2})	3	19	28	28	5
N_c (10^{12} cm^{-2})	4	25	44	44	15
ε (10^{-3})	6	15	18	18	8
FWHM	0.4338	0.3524	0.4132	0.4132	0.1771
d (Å)	3.11	3.08	3.17	3.15	3.19

other concentration. Consequently, this enhancement leads to lesser crystal defects and for small recombination centers at the grain boundaries. Additionally, micro-strain and dislocation densities calculated to investigate the film quality such as crystal defects, dislocations and the presence of lattice imperfections. Therefore, we can say that CATS deposited with high quality and lesser defects, where δ_{dis} and N_c were equal to $5*10^{11}$ cm^{-2} and $15*10^{12}$ cm^{-2} respectively.

XRD data used to evaluate Lattice parameters ‘a’ and ‘c’, Unit cell volume (V), Molecular weight (M), X- ray density (d_x) and Porosity (P) from the following expressions (Somvanshi et al., 2020):

$$a = d\sqrt{h^2 + k^2 + \frac{a^2}{c^2}l^2} \quad V = a^2 \times c$$

$$dx = \frac{Z \times M}{V \times N_A}, \quad P = 1 - \frac{d_B}{d_x} \tag{3}$$

where, d, (h, k, l), M, Z, N_A and d_B are the inter-planar spacing, miller indices, molecular weight, atoms number per unit cell, Avogadro’s number and bulk density, respectively. The structural parameters are tabulated in Table 3. Generally, it is found that Al concentration promotes a remarkable increment of lattice parameters ‘a’ and ‘c’ that correlated with the shift of diffraction peaks toward lower angles. Consequently, ‘a’ and ‘c’ lead to increase in the unit cell volume that decreases the X- ray density. Notably, the highest film porosity found for CATS film may be ascribed to the presence of major void space.

3.3. Raman spectroscopy

XRD patterns of all chalcogenides Cu_2XSnS_4 (where X is a metal) are similar and close to that of FeS and Cu_3SnS_4 (Mokurala et al., 2016). Raman spectroscopy utilized 488 nm as excitation wavelength and shown in Fig. 3. As mentioned from our previous work and literature (Nefzi et al., 2018), quaternary chalcogenides show principally two Raman peaks. For example, CFTS is kknown to show two Raman peaks at 285 cm^{-1} and 319 cm^{-1}, which are observed here. Fig. 3 demonstrates that CATS displays two principal peaks at 335 cm^{-1} and 295 cm^{-1} which may be identified as the A_1 and the B/E modes respectively. In our knowledge, there is no work, which identified the Raman peaks of CATS material before. As a consequence, Raman peak matched at 295 cm^{-1}

Table 3 Values of interplanar distance d, unit cell volume (V), molecular weight (M), X-ray density (d_x) and porosity (P) of $Cu_2Fe_{1\text{-}x}Al_xSnS_4$ ($0 \leq x \leq 1$) thin films.

x	d (112)(Å)	d (204) (Å)	V (Å^3)	M (g mol^{-1})	$d_x \times 10^{-23}$ (g/Å^3)	P(%)
0	3.1161	1.9056	313.1	430	3.66	34
0.25	3.0899	1.9881	310.2	423	3.62	35
0.50	3.1625	1.9301	329.3	415	3.35	37
0.75	3.1724	1.9241	329.2	408	3.29	38
1	3.1898	1.9364	337.3	401	3.16	43

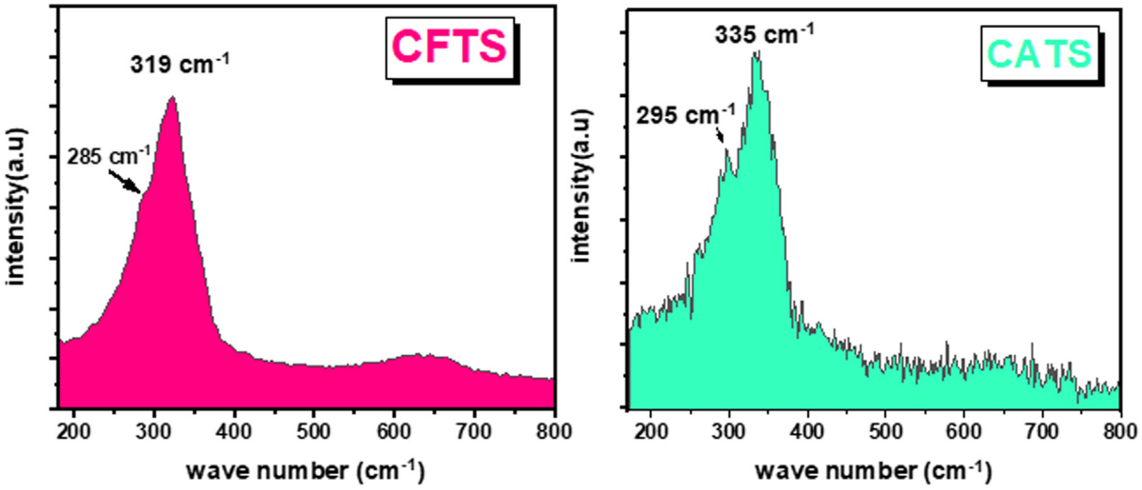

Fig. 3 Raman scattering results for CFTS and CATS films.

may correspond to S^{2-} around Cu^{2+} (Lee et al., 2012). Then, the principal peak at 335 cm^{-1} may be attributed to the strongest asymmetric vibrational mode of S^{2-} around Sn (Lee et al., 2012).

3.4. Morphological analysis

Fig. 4 shows the morphological states of CFATS thin layers (x = 0 – 0.25 – 0.50–0.75 and 1) extracted from SEM, revealing a transformation in film morphology. It is evident that Cu_2FeSnS_4 film appears with smooth and uniform surface. At x = 0.25, it is clear that the surface morphology is uniform and dense with some cracks. A granulated structure with small grain size distribution was observed at x = 0.50. The micrographs at x = 0.75 reveal that the film surface is covered with large numbers of rod-shaped grains that are closely attached to each other. By contrast, the surface morphology of CATS appears as well as a nanofibers structure accompanied with voids and cavities. This trend is beneficial for photovoltaic applications as motioned by Hao Guan et al. (Guan et al., 2014). These obtained results are similar to those reported in other researches (Guan et al., 2014; Ozel et al., 2015). Fig. 5 indicates that film thickness of CATS slightly decreased to 723 nm compared to CFTS which mainly associates with the decrease of crystallite size.

3.5. Optical properties

The optical band gap (Eg) of sprayed CFATS thin films was deduced by utilizing Tauc's relationship (Jrad et al., 2016):

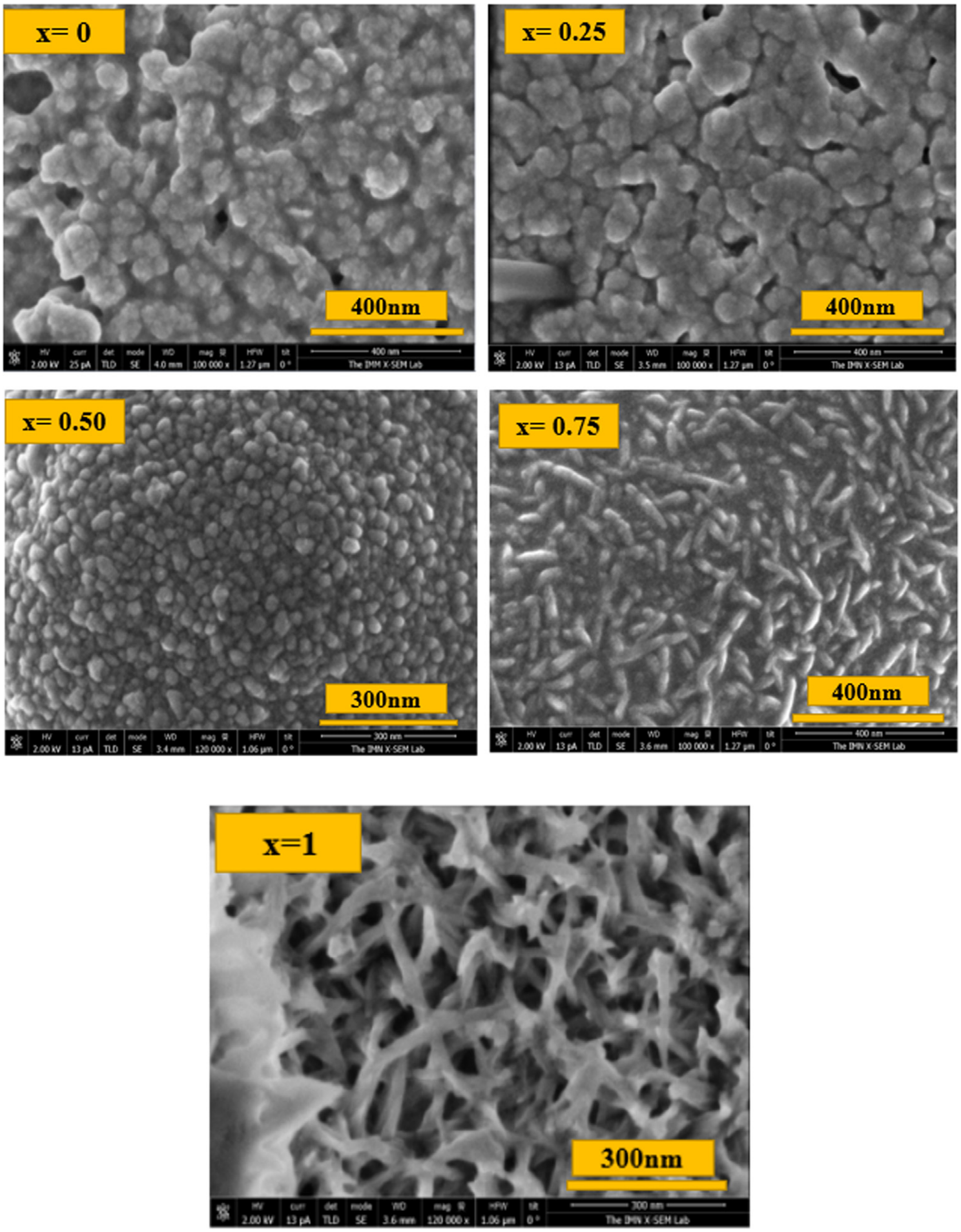

Fig. 4 Morphology of the as-synthesized $Cu_2Fe_{1-x}Al_xSnS_4$ (CFATS) films (x = 0 – 0.25 – 0.50–0.75 and 1).

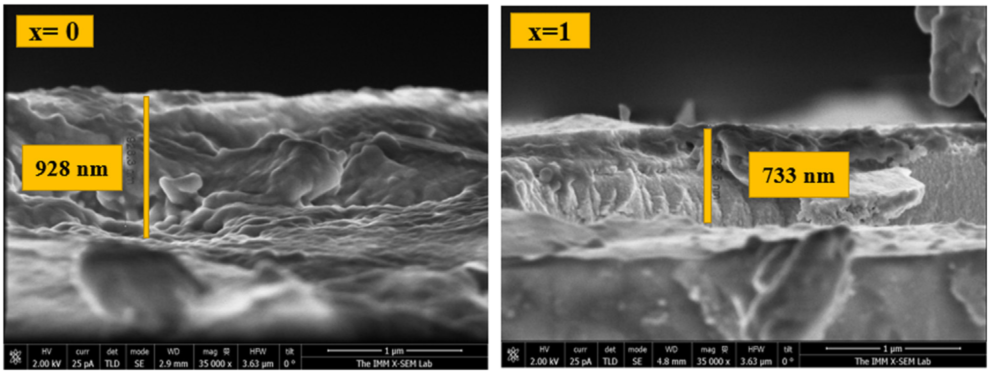

Fig. 5 Cross-section views of CFTS and CATS films for scale of 1 µm.

$$(\alpha \mathbf{h}\nu) = \mathbf{A}(\mathbf{h}\nu - \mathbf{Eg})^{\mathbf{n}} \qquad (4)$$

Where A is a constant and n presents the nature of transition. After fitting, all $Cu_2Fe_{1\text{-}x}Al_xSnS_4$ layers were found to obey equation (3) with n = 2, which presents the direct transition type as shown in Fig. 6. Generally, the molarity of Al in the solution precursors affects the optical band gap values of elaborated CFATS thin films. The optical band gap of CFATS was varied with incorporating more Al atoms in the Fe lattices. This increment is due to the modification in composition and surface morphology (Fig. 4; Table 1). Eg is found to be increased from 1.47 eV to a maximum value about 2.1 eV with decrement of crystallite size, which may be attributed to the quantum confinement effect (Beraich et al., 2020). The films grown at x = 0.50 and 1 with optimum band gaps are well suited to be used as absorber layers in solar cell applications. In addition, the increase in Eg can also be originated to the less structural defects in samples that accompanied by the decrease in the density of defect states due to the decrease in film thickness of CFATS, as well as during the growth process. Hence, the optical band gap Eg = 1.52 eV of CATS is tuned to make it optically active as absorber layer for solar cell application.

3.6. Wettability measurement

The surface wettability of materials is considered as a significant parameter to exploring their performance. It let to investigate the difference of energy between the molecules, which exist on the surface and those of material. Thomas Young described the contact angle θ_Y in 1805 using the following equation (Ben Ameur et al., 2020):

$$\cos\boldsymbol{\theta}_{Y} = \frac{\gamma_{SV} - \gamma_{SL}}{\gamma_{LV}} \qquad (5)$$

Where γ_{SV}, γ_{LV}andγ_{SL} correspond to the interfacial tensions with solid/vapor, liquid/vapor and solid/liquid respectively. Fig. 7 presents water contact form on CFATS thin layers. It is clear that CFATS thin films exhibit a hydrophilic character with $\theta_Y < 90^{\circ}$. According to the curve, after inclusion of aluminum atoms, CATS (x = 1) material exhibits lowest contact angle near 44.6°, because CATS appears as nanofibers accompanied with voids and cavities. As stated by the figure, the droplets on materials surface exhibited elliptical form. The surface wetting behavior is controlled by various parameters such as micro/nanotexture and chemical composition. The variation of water contact angle θ_Y is related to the change of surface free energy and surface morphology. It can also be explained by the weak adhesive force accompanied with Van der Waals forces between the water and material surfaces (Geim et al., 2003). However, it has been demonstrated that films with hydrophilic character produce large surface area between solid and liquid (Mrabet et al., 2016). This surface type favors the physisorption processes, which are necessary for antibacterial and photocatalytic activities (Dridi et al., 2017).

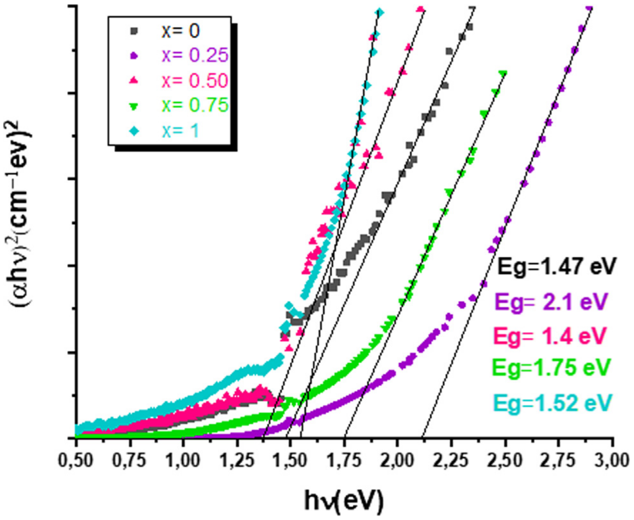

Fig. 6 Tauc-plot of the as-deposited $Cu_2Fe_{1\text{-}x}Al_xSnS_4$ (CFATS) films (x = 0–0.25 – 0.50–0.75 and 1).

3.7. Cyclic voltammetry (CV) analysis

See Fig. 8a represents the cyclic voltammogram plot for CATS thin layer.The electrochemical energy level of CATS thin film was extracted from the first oxidation onset potentials peak. It is shown that the valance-band edge (VB) equals to 0.29 eV. Conduction-band edge was given from the following expression: $E_{CB} = E_{VB} - Eg$, whereas $E_{VB} = 0.29$ eV and $E_g = 1.52$ eV so $E_{CB} = -1.23$ eV. From our previous work (Nefzi et al., 2020c), the valence and conduction band edges of SnO_2:F were located respectively at −3.96 eV and 0.1 eV.

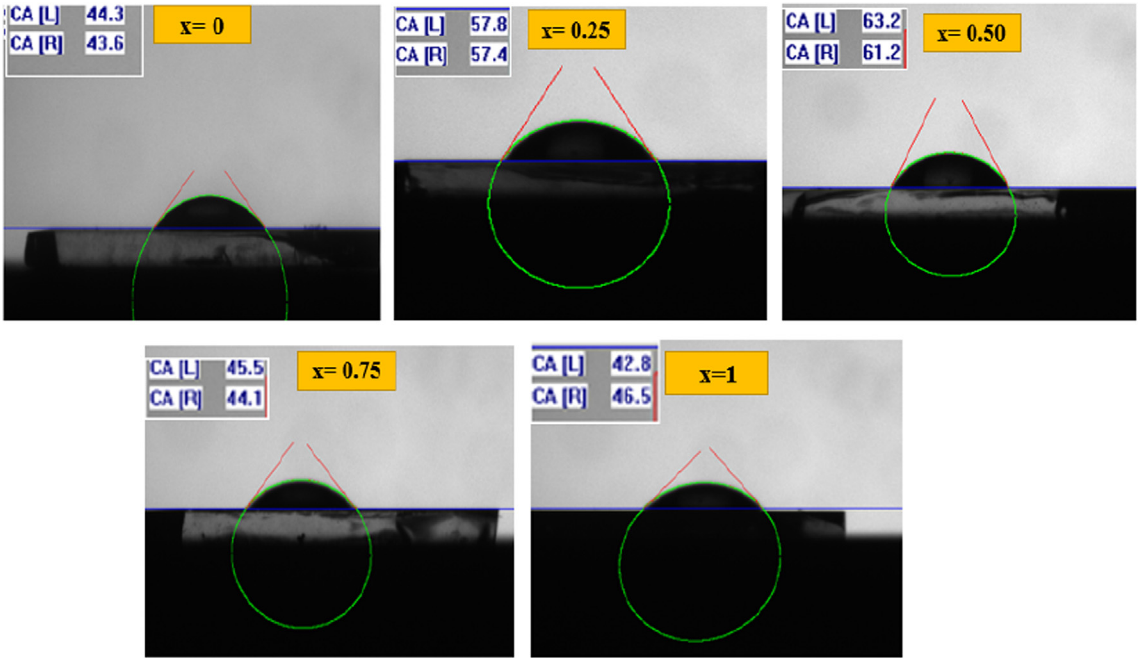

Fig. 7 Water contact angle of $Cu_2Fe_{1-x}Al_xSnS_4$ (CFATS) films deposited by spray pyrolysis (x = 0–0.25 – 0.50–0.75 and 1).

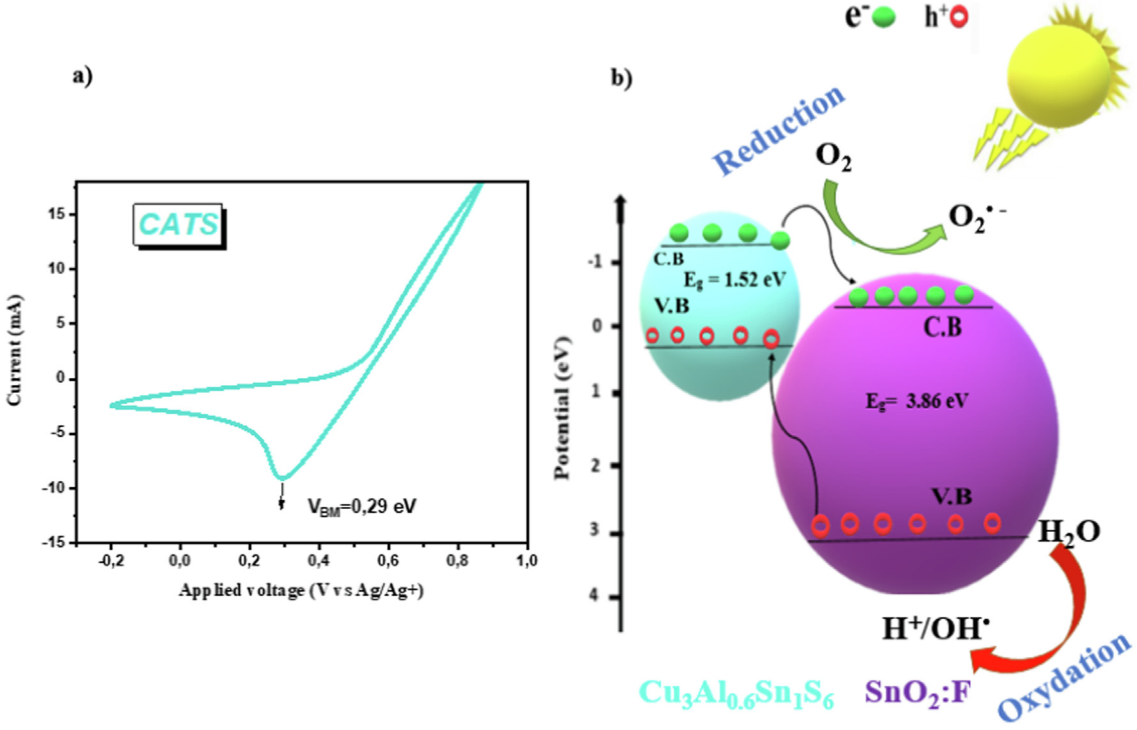

Fig. 8 a) Cyclic voltammogram of CATS thin film, b) Mechanism of visible light antibacterial activity of CATS/SnO_2:F heterojunction.

3.8. Antibactetrial and hydrophilicity properties

Antibacterial tests were carried on *Escherichia coli* (*E.coli*) and *Staphylococcus aureus* (*S. aureus*) because they are culprits in various infections. The antibacterial activities of SnO_2:F, CATS films and CATS/SnO_2:F heterojunction against the degradation of *E. coli* and *S. aureus* were examined, and the results are presented in Fig. 9a. The evaluation of antibacterial activity has been performed by counting forming unity (CFU). SnO_2:F and CATS films exhibit stronger antibacterial activities for Gram positive *S. aureus* than that of Gram negative *E. coli*, while the opposite trend was found for CATS/SnO_2:

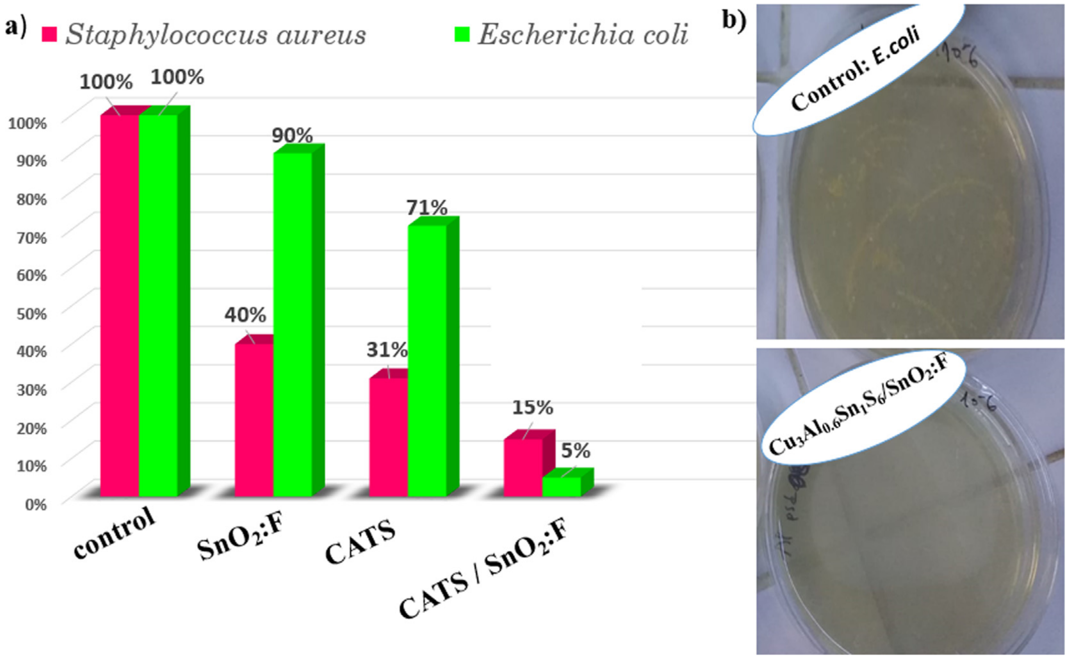

Fig. 9 Percentage of bacterial inhibition of E. coli and S. aureus bacteria against SnO_2:F and CATS films and CATS/SnO_2:F heterojunction by monitoring the optical density (OD) at 600 nm. Antibacterial activity assay of CATS/SnO_2:F heterojunction against E. coli.

F heterojunction. These behaviors are due to the antibacterial mechanisms of films and the different bacteria structures (Qi et al., 2019). Generally, a greater inhibition of both *S. aureus* and *E. coli* was attained by CATS/SnO_2:F heterojunction which may be attributed to its fast carriers generation (Ali et al., 2020). Deposition of p-type CATS on the surface of n-type SnO_2:F caused generation of the space charge layer (SCL) that affected the charge carriers diffusion. Therefore, it will increase the negative and positive carrier's separation. The viability rates achieved against *S. aureus* was 40 %, 31 %, and 15% for SnO_2:F, CATS films and CATS/SnO_2:F heterojunction, indicating the excellent results of antibacterial activity of coupled CATS/SnO_2:F. A poor inhibition of *E. coli* bacterium implying just 90 % and 71% reductions to the surface of SnO_2:F and CATS films. However, CATS/SnO_2:F heterojunction has good effect in the antibacterial activity reaching 5 % as viability rate of *E. coli*. It has been proposed that the cation released from materials (in our case $Cu^{2+}_{,}$ Al^{3+} and Sn^{2+}) could bind to thiol groups (SH) found in proteins and enzymes on the surface of cellule. Then, they can intervene in with cell division and conductive to bacterial cell death (Shao et al., 2015). Antibacterial activity assay of the membranes by CATS/SnO_2:F heterojunction against the degradation of *E. coli* and *S. aureus* are shown in Fig. 9b.

See Fig. 8b reports the antibacterial activity mechanism of CATS/SnO2:F heterojunction. Beside, CATS presents narrow band gap, the electron can jumped from its valance-band (VB) to its conduction band (CB) by the generation of same contents of holes in its VB. The photogenerated electrons located in CB of CATS can migrate to the CB of SnO_2:F, because of the more positive CB of SnO_2:F than that of CATS. Therefore, the photogenerated holes located at the VB of SnO_2:F achieve the VB of CATS. Thus, the efficient charge separation enhances the lifetime of charge carriers, increasing the reduction and oxidation process that produce the reactive oxygen species (ROS). Meanwhile, the death of bacteria is mostly ascribed to the destruction of their outer membrane. The crust damage instigated by physical or chemical modification of the surface membrane because it consists of lipid along a polyunsaturated fatty acid (Ali et al., 2020). Then, a reaction of free radicals with polyunsaturated acids and initiation of lipid peroxide formation modifies the fluidity of membrane and interrupts protein bonds. This rapid augmentation of radicals induces oxidative stress that results in the degradation of polyunsaturated fatty acids in harmful products (Ali et al., 2020). CATS/SnO_2:F heterojunction is easy to penetrate the cell wall of *E. coli* than *S. aureus*, SnO_2:F and CATS films present lower antibacterial activity to *E. coli*.

3.9. Correlation between antibactetrial and hydrophilicity

It has been demonstrated here that CATS was characterized with hydrophilic surface. This surface type may be caused by the nanofiber structure accompanied with voids and cavities, which have been clearly observed in SEM images. It has been already established in the literature (De Falco et al., 2018; Qi et al., 2019; Karam et al., 2013), that materials with hydrophilic surfaces display higher antibacterial activity than those with hydrophobic surfaces. Contrary to the mechanism that conduct wettability, holes which exist in the valence band react with the adsorbed H_2O to generate hydroxyl radicals, whereas electrons contribute to reduction processes with oxygen molecules generating superoxide anions O^{2-} (Chen et al., 2012; Cho et al., 2004). Such responsible species for the inactivation of bacteria through oxidative damages (Cai et al., 2014) are also capable in damaging the cytoplasmic membrane and the outer membrane of microorganisms, consequently, deteriorate essential cellular components leading to cell death.

4. Conclusion

In summary, a simple and facile method was developed to synthesize $Cu_2Fe_{1-x}Al_xSnS_4$ (CFATS). The aluminum content was varied to obtain new quaternary chalcogenide named CATS. XRD spectra and EDX revealed the formation of this new quaternary $Cu_3Al_{0.6}Sn_1S_6$ chalogenide which crystalized with stannite structure. Two Raman peaks located at 335 cm^{-1} (A_1-mode) and 295 cm^{-1} (B/E mode) have been assigned to CATS material. A nanofiber structure coupled with voids and cavities was noted in SEM image of CATS, prompting us to investigate the antibacterial properties of CATS film and improve its antibacterial activity by coupling it with SnO_2:F. This novel chalcogenide features optimum band gap near 1.52 eV, which renders it as absorber layer for photovoltaic application. CATS grows with the high porosity, explicating its hydrophilic surface and provides a way for the possibilities of using CATS in several applications such as self-disinfecting and self-cleaning. Overall, this work reveals also that the surface of CATS/SnO_2:F heterojunction displayed higher inhibition against *S. aureus* and *E. coli* bacteria.

Acknowledgments

The authors would like to acknowledge the Deanship of Scientific Research at Umm Al-Qura University for supporting this work by Grant code: 22UQU4350568DSR01. Also, the author would thank Dr. Ziad Moussa, United Arab Emirates University, as native English specker (Canadian) for his valuable editing and revision the manuscript

References

Agawane, G.L., Shin, S.W., Vanalakar, S.A., Moholkar, A.V., Kim, J. H., 2014. Next generation promising $Cu_2(ZnxFe_{1-x})SnS_4$ photovoltaic absorber material prepared by pulsed laser deposition technique. Mater. Lett. 137, 147–149.

Ali, A., Liang, Y., Ahmed, S., Yang, B., Guo, B., Yang, Y., 2020. Mutual contaminants relational realization and photocatalytic treatment using Cu_2MgSnS_4 decorated $BaTiO_3$. Appl. Mater. Today 18, 100534.

Amoupour, E., Hassnzadeh, J., Ziabari, A.A., Anaraki, P.A., 2021. Numerical simulations of ultrathin CdTe solar cells with a ZnxCd1−xS window layer and a Cu_2O hole transport layer. J. Comput. Electron. 20, 2501–2510.

Ben Ameur, S., Duponchel, B., Leroy, G., Maghraoui-Meherzi, H., Amlouk, M., Guermazi, H., Guermazi, S., 2020. Impact of substrate nature and film thickness on physical properties of antimony trisulphide (Sb_2S_3) thin films for multifunctional device applications. Superlattices Microstruct. 142, 106473.

Benyahia, K., Djeffal, F., Ferhati, H., Benhaya, A., Bendjerad, A., Djaballah, Y., Martin, N., 2021. Microstructured ZnO-ZnS composite for earth-abundant photovoltaics: elaboration, surface analysis and enhanced optical performances. Sol. Energy 218, 312–319.

Beraich, M., Taibi, M., Guenbour, A., Zarrouk, A., Bellaouchou, A., Fahoume, M., 2020. Synthesis of tetragonal Cu_2NiSnS_4 thin film via low-cost electrodeposition method: effect of Ni^{2+} molarity. J. Electron. Mater. 49, 728–735.

Betul, T., Sergiu, L., Hannes, H., Eric, B., José, A.M., Leo, C., Ian, G. H., Thomas, U., David, B.M., 2021. Optoelectronic and material properties of solution-processed Earth-abundant $Cu_2BaSn(S, Se)_4$ films for solar cell applications. Nano Energy 80, 105556.

Cai, Y., Strømme, M., Welch, K., 2014. Disinfection kinetics and contribution of reactive oxygen species when eliminating bacteria with TiO2 induced photocatalysis. J. Biomater. Nanobiotechnol. 5, 200.

Chen, H., Nanayakkara, C.E., Grassian, V.H., 2012. Titanium dioxide photocatalysis in atmospheric chemistry. Chem. Rev. 112, 5919–5948.

Cho, M., Chung, H., Choi, W., Yoon, J., 2004. Linear correlation between inactivation of E. coli and OH radical concentration in TiO2 photocatalytic disinfection. Water Res. 38, 1069–1077.

Das Bakshi, S., Sinha, D., Ghosh Chowdhury, S., 2018. Anisotropic broadening of XRD peaks of α'-Fe: Williamson-Hall and Warren-Averbach analysis using full width at half maximum (FWHM) and integral breadth (IB). Mater. Charact. 142, 144–153.

Davarpanah, M., Bakhtiari, R., Karimi, M., Hosseini, S.F., Esmaeili, A., 2022. Iranian native medicinal plants affecting staphylococcus aureus as septic pathogens. Egypt. J. Vet. Sci. 53, 1–8.

De Falco, G., Ciardiello, R., Commodo, M., Del Gaudio, P., Minutolo, P., Porta, A., D'Anna, A., 2018. TiO2 nanoparticle coatings with advanced antibacterial and hydrophilic properties prepared by flame aerosol synthesis and thermophoretic deposition. Surf. Coat. Technol. 349, 830–837.

Dridi, R., Mrabet, C., Labidi, A., Mahdhi, N., Amlouk, A., Amlouk, M., 2017. Electrical conductivity of Zn2SnO4 thin films along with wettability and EtOH-sensing. J. Alloy. Compd. 708, 769–779.

Geim, A., Dubonos, S., Grigorieva, I., Novoselov, K., Zhukov, A., Shapoval, S.Y., 2003. Microfabricated adhesive mimicking gecko foot-hair. Nat. Mater. 2, 461–463.

Guan, H., Shen, H., Jiao, B., Wang, X., 2014. Structural and optical properties of Cu2FeSnS4 thin film synthesized via a simple chemical method. Mater. Sci. Semicond. Process. 25, 159–162.

Hussein, Z., Laref, A., Alqahtani, H.R., Alghamdi, E.A., Monir, M. A., Noor, N.A., Huang, H.M., Xiong, Y.C., Yang, J.T., Yakou, H. A., 2021. Optoelectronic properties of solar cell materials based on copper-zinc-tin-sulfide Cu2ZnSn(SxTe1-x)4 alloys for photovoltaic device applications. Sol. Energy 225, 851–862.

Jrad, A., Naffouti, W., Nefzi, C., Ben Nasr, T., Ammar, S., Turki-Kamoun, N., 2016. Effect of copper concentration on the physical properties of ZnS: Cu alloys prepared by chemical bath deposition. J. Mater. Sci.: Mater. Electron. 27, 10684–10695.

Karam, L., Jama, C., Mamede, A.-S., Boukla, S., Dhulster, P., Chihib Nisin, N.-E., 2013. Activated hydrophobic and hydrophilic surfaces: assessment of peptide adsorption and antibacterial activity against some food pathogens. Appl. Microbiol. Biotechnol. 97, 10321–10328.

Khemiri, N., Chamekh, S., Kanzari, M., 2020. Properties of thermally evaporated CZTS thin films and numerical simulation of earth abundant and non toxic CZTS/Zn(S, O) based solar cells. Sol. Energy 207, 496–502.

Kim, T., Park, C., Samuel, E.P., An, S., Aldalbahi, A., Alotaibi, F., Yarin, A.L., Yoon, S.S., 2021. Supersonically sprayed washable, wearable, stretchable, hydrophobic, and antibacterial rGO/AgNW fabric for multifunctional sensors and supercapacitors. ACS Appl. Mater. Interfaces 13, 10013–10025.

Koç, M.M., Dere, A., Özdere, A., Al-Sehemi, A.G., Coskun, B., Al-Ghamdi, A.A., Erkovan, M., Yakuphanoglu, F., 2021. Optoelectronic investigation of Cu2FeSnS4 quaternary functional photodiodes with IR detection capabilities. J. Mol. Struct. 1246, 131265.

Lee, W.J., Lee, J.M., Kochuveedu, S.T., Han, T.H., Jeong, H.Y., Park, M., Yun, J.M., Kwangsoo, J.K., Kim, D.H., Kim, S.O., 2012. Biomineralized N-doped CNT/TiO2 core/shell nanowires for visible light photocatalysis. ACS Nano 6, 935–943.

Mokurala, K., Mallick, S., Bhargava, P., 2016. Alternative quaternary chalcopyrite sulfides (Cu_2FeSnS_4 and Cu_2CoSnS_4) as electrocatalyst materials for counter electrodes in dyesensitized solar cells. J. Power Sources 305, 134–143.

Monisha, P., Priyadharshini, P., Gomathi, S.S., Pushpanathan, K., 2021. Influence of Mn dopant on the crystallite size, optical and magnetic behaviour of $CoFe_2O_4$ magnetic nanoparticles. J. Phys. Chem. Solids 148, 109654.

Mrabet, C., Mahdhi, N., Boukhachem, A., Amlouk, M., Manoub, T., 2016. Effects of surface oxygen vacancies content on wettability of zinc oxide nanorods doped with lanthanum. J. Alloy. Compd. 688, 122–132.

Naderi, E., Akbarzadeh, N., Kondori, T., Tahkor, A., 2020. Preparation and identification of nanoparticle of lanthanum oxide and its application as antibacterial agent. Eurasian Chem. Commu., 265–271

Nefzi, C., Askri, B., Dabaki, Y., García, J.M., Kamoun-Turki, N., 2021a. Synthesis of new promising quaternary Cu2InSnS4 absorber layer: physical behaviors, wettability and photocatalysis applications. J. Alloy. Compd. 162771.

Nefzi, C., Souli, M., Dotor Castilla M.L., Garcia, J.M., Kamoun-Turki, N., 2020c. CFTS-3/In2S3/SnO2:F heterojunction structure as eco-friendly photocatalytic candidate for removing organic pollutants. Arab. J. Chem. 13, 6366–6378.

Nefzi, C., Souli, M., Cuminal, Y., Kamoun-Turki, N., 2018. Effect of sulfur concentration on structural, optical and electrical properties of Cu_2FeSnS_4 thin films for solar cells and photocatalysis applications. Superlattices Microstruct. 124, 17–29.

Nefzi, C., Souli, M., Cuminal, Y., Kamoun-Turki, N., 2020a. Effect of substrate temperature on physical properties of Cu2FeSnS4 thin films for photocatalysis applications. Mater. Sci. Eng., B 254, 114509.

Nefzi, C., Souli, M., Costa-Krämer, J.L., García, J.M., Kamoun-Turki, N., 2020b. Growth of the next generation promising Cu2 Fe1-xCoxSnS4 thin films and efficient p-CCTS/n-In_2S_3/n-SnO_2F heterojunction for optoelectronic applications. Mater. Res. Bull. 133, 111028.

Nefzi, C., Yahmadi, B., El Guesmi, N., García, J.M., Kamoun-Turki, N., Ahmed, S.A., 2021b. Exploitation of irradiated Cu2InSnS4 semiconductor: a successful attempts with high efficacy towards water treatment under photocatalysis approach. J. Mol. Struct. 131943.

Orletskii, I.G., Maryanchuk, P.D., Solovan, M.N., Maistruk, E.V., Kozyarskii, D.P., 2018. Electrical and optical properties of Cu_2Zn (Fe, Mn)Sn_S4 films prepared by spray pyrolysis. Optics 63, 251–257.

Ozel, F., 2016. Earth-abundant quaternary semiconductor Cu2MSnS4 (M = Fe Co, Ni and Mn) nanofibers: fabrication, characterization and band gap arrangement. J. Alloy. Compd. 657, 157–162.

Ozel, F., Kus, M., Yar, A., Arkan, E., Can, M., Aljabour, A., Varal, N.M., Ersoz, M., 2015. Fabrication of quaternary Cu_2FeSnS_4 (CFTS) nanocrystalline fibers through electrospinning technique. J. Mater. Sci. 50, 777–783.

Qi, Y., Ma, H.-L., Du, Z.-H., Yang, B., Wu, J., Wang, R., Zhang, X.-Q., 2019. Hydrophilic and antibacterial modification of poly(lactic acid) films by γ–ray irradiation. ACS Omega 4, 21439–21445.

Sadanand, Singh, P.K., Rai, S., Lohia, P., Dwivedi, D.K., 2021. Comparative study of the CZTS, $CuSbS_2$ and $CuSbSe_2$ solar photovoltaic cell with an earth-abundant non-toxic buffer layer. Solar Energy 222, 175–185.

Shao, W., Liu, X., Min, H., Dong, G., Feng, Q., Zuo, S., 2015. Preparation, characterization, and antibacterial activity of silver nanoparticle-decorated graphene oxide nanocomposite. ACS Appl. Mater. Interfaces 7, 6966–6973.

Shin, B., Gunawan, O., Zhu, Y., Bojarczuk, N.A., Chey, S.J., Guha, S., 2013. Thin film solar cell with 8.4% power conversion efficiency using an earth-abundant Cu_2ZnSnS_4 absorber. Prog. Photovoltaics Res. Appl. 21, 72–76.

Shin, M.J., Lee, A., Park, J.H., Cho, A., Ahn, S.K., Shin, D., Gwak, J., Yun, J.H., Yoo, J., Cho, J.-S., 2022. Ultrathin Cu(In, Ga)S_e2 transparent photovoltaics: an alternative to conventional solar energy-harvesting windows. Nano Energy 92, 106711.

Somvanshi, S.B., Patade, S.R., Andhare, D.D., Jadhav, S.A., Khedkar, M.V., Kharat, P.B., Khirade, P.P., Jadhav, K.M., 2020. Hyperthermic evaluation of oleic acid coated nano-spinel magnesium ferrite: enhancement via hydrophobic-to-hydrophilic surface transformation. J. Alloy. Compd. 835, 155422.

Sopata, M., Karpinski, T.M., Jakubowicz, J., Sopata, M., 2020. Development of tantalum with highly hydrophilic surface and antimicrobial properties obtained by micro-arc oxidation process. J. Biomed. Mater. Res., 1–12

Sui, S., Li, L., Shen, J., Ni, G., Xie, H., Lin, Q., Zhao, Y., Guo, J., Duan, W., 2020. Plasma treatment of polymethyl methacrylate to improve surface hydrophilicity and antifouling performance' wileyonlinelibrary. Soc. Plastics Eng., 1–8

Sun, K., Wang, A., Su, Z., Liu, F., Hao, X., 2021. Enhancing the performance of Cu_2ZnSnS_4 solar cell fabricated via successive ionic layer adsorption and reaction method by optimizing the annealing process. Sol. Energy 220, 204–210.

Venkatachalam, S., Iida, Y., Kanno, Y., 2008. Preparation and characterization of Al doped ZnO thin films by PLD. Superlattices Microstruct. 44, 127–135.

Victoria, M., Haegel, N., Peters, I.M., Sinton, R., Jäger-Waldau, A., del Cañizo, C., Breyer, C., Stocks, M., Blakers, A., Kaizuka, I., Komoto, K., Smets, S., 2021. Solar photovoltaics is ready to power a sustainable future, Joule 5, 1041–1056, May 19, 1043.

Wan, Y., Wang, Z., Xu, Z., Liu, C., Zhang, J., 2011. Fabrication and wear protection performance of superhydrophobic surface on zinc. Appl. Surf. Sci. 257, 7486–7489.

Wang, P., Zhang, D., Qiu, R., Hou, B., 2011. Super-hydrophobic film prepared on zinc as corrosion barrier. Corros. Sci. 53, 2080–2086.